Effects of Reaction Temperature and Raw Material Type on Optical Properties and Crystal Phase Growth of Solid State Synthesized $NiSb_2O_6$ Nanomaterials

Alireza Hakimyfard *

Department of Basic science, Jundi-Shapur University of Technology, Dezful, Iran.

ARTICLE INFO

Article history:

Received 11 August 2017
Accepted 25 November 2017
Available online 15 March 2018

Keywords:

$NiSb_2O_6$
Solid state
Nanomaterial
Rietveld

ABSTRACT

Nanostructured $NiSb_2O_6$ samples were synthesized via solid state reactions at 600, 700 and 800 °C using Sb_2O_3, $Ni(CH_3COO)_2.2H_2O$ and $Ni(NO_3)_2.6H_2O$ as the raw materials. Parameters of reaction temperature and raw material type were investigated for the crystal phase growth study. The synthesized nanomaterials were characterized by X-ray powder diffraction (XRPD) technique, fourier-transform infrared (FTIR) spectroscopy. Brunauer–Emmett–Teller (BET) and Barrett-Joyner-Halenda (BJH) methods were used to investigate the textural properties of the obtained samples. Rietveld analyses showed that the obtained materials were crystallized well with a tetragonal crystal structure with the space group of $P4_2/mnm$. The lattice parameters of the targets were about a = b = 4.64 Å and c = 9.22 Å. The data revealed that the crystal phase purity of the as-synthesized nanomaterials increased with raising the reaction temperature from 600 to 800 °C. Besides, the data indicated that the synthesis reactions using $Ni(NO_3)_2.6H_2O$ generated a better crystalline growth and purity compared to $Ni(CH_3COO)_2.2H_2O$ raw material in a certain reaction temperature. The morphologies of the synthesized materials were studied by field emission scanning electron microscopy (FESEM) technique. The FESEM images showed that the homogeneity of the synthesized powder was improved when $Ni(NO_3)_2.6H_2O$ was used as the raw material. Ultraviolet-visible spectra showed that the synthesized $NiSb_2O_6$ nanomaterials had a strong light absorption in the ultraviolet light region. The calculated direct optical band gaps tendency showed that the band gaps increased with increasing the reaction temperature.

1-Introduction

Transition metal antimonates, with the general formula MSb_2O_6 (M = Zn, Cd, Pb, Ni, etc.), have been investigated primarily because of their interesting structure, electronic, and optical properties. These oxides crystallize in the trirutile crystal structure in the space group of P42/mnm. $NiSb_2O_6$ has attracted attention due to its magnetic photocatalytic, as transparent conductor, and sensors properties [1]. It finds applications as metal oxide–antimony catalyst and in resistors [2-4]. Several methods have been reported for the synthesis of $NiSb_2O_6$ materials including solid state method using $NiSO_4$ and $NaSbO_3$ at 500 °C [1], solid state method using NiO and Sb_2O_4 at 900 °C [2], sol-gel method [4,5], hydrothermal method [6], solid state method using Sb_2O_3 and NiO at 800 °C for 72 h

* Corresponding author:
E-mail address: ahakimyfard@jsu.ac.ir

[7], solid state method using NiO and Sb_2O_3 at 1450 °C for 48h [8], and microwave - assisted colloidal method [9]. However, the hydrothermal method is a versatile route for the synthesis of nanostructured materials [10, 11], but the present study utilized a simple solid state route for the first time to synthesize nanostructured $NiSb_2O_6$ powders using Sb_2O_3, $Ni(CH_3COO)_2.2H_2O$ and $Ni(NO_3)_2.6H_2O$ raw materials. Rietveld analysis was used for investigation of crystal phase growth and purity of the obtained nanomaterials. The textural analysis was done by BET and BJH analyses. The direct optical band gaps were calculated using UV-Vis spectra and related to the reaction temperature.

2- Experimental

2-1- Materials and methods

All chemicals including Sb_2O_3, $Ni(CH_3COO)_2.2H_2O$ and $Ni(NO_3)_2.6H_2O$ were of analytical grade and were obtained from commercial sources (Merck Co., Germany) and used without further purifications. Phase identification was performed by a powder X-ray diffractometer D5000 (Siemens AG, Munich, Germany) using Cu-K_α radiation. The Rietveld analysis was done by FullProf software. The surface area and pore volume and average nanoparticles size were calculated using the Brunauer-Emmett-Teller (BET) equation. Pore size distributions, pore volume and pore surface area were calculated by the Barrett-Joyner-Halenda (BJH) method. The BET surface areas were acquired on a Beckman Coulter SA3100 Surface Area Analyzer. The morphology of the obtained materials was examined by a field emission scanning electron microscope (Hitachi FE-SEM model S-4160). FTIR spectra were recorded on a Tensor 27 (Bruker Corporation, Germany). The absorption spectra were recorded on a UV-visible spectrophotometer model-UV-1650 PC (Shimadzu, Japan).

2-2- Solid state synthesis of $NiSb_2O_6$ nanopowders

In a typical experiment, 0.25 g (1 mmol) of $Ni(CH_3COO)_2.2H_2O$ (MW = 250.0 $gmol^{-1}$) and 0.292 g (1 mmol) of Sb_2O_3 (MW = 291.5 $gmol^{-1}$) were mixed in a mortar and ground until a nearly homogeneous powder was obtained. The obtained powder was poured into a 25 mL ceramic crucible and treated thermally in one step at 600 ˚C (S_1), 700 °C (S_3) and 800 °C (S_5) for 8 h. The crucible was then cooled normally in the furnace to the room temperature. The obtained powders were collected for further analyses.

In another synthesis experiment, the above mentioned experimental process was used. The only difference between the two processes is the nickel (II) salt raw material type. For this purpose, 0.297 g (1 mmol) of $Ni(NO_3)_2.6H_2O$ (MW = 290.7 $gmol^{-1}$) and 0.292 g (1 mmol) of Sb_2O_3 (MW = 291.5 $gmol^{-1}$) were used. The synthesis reactions were performed at 600 °C (S_2), 700 °C (S_4) and 800 °C (S_6) for 8 h. The syntheses yields for $NiSb_2O_6$ (MW= 398.21 $gmol^{-1}$) were 0.28 (70 %), 0.32 g (80 %) and 0.34 g (85 %) and 0.37 g (93 %) for S_3, S_4, S_5 and S_6, respectively.

3- Results and discussion

3-1- Characterization

The XRPD patterns of the $NiSb_2O_6$ samples are reported in Fig. 1 as the data points, together with the result of the profile matching analysis (full lines). Fig. 1 shows the XRPD analyses of the obtained $NiSb_2O_6$ samples in the θ-2θ geometry with Cu-Kα radiation. Structural analyses were done by the FullProf program by employing profile matching with a constant scale factor. The results showed that the patterns had a main $NiSb_2O_6$ tetragonal crystal structure with the space group of $P4_2/mnm$ [7-9, 12, 13]. According to the Rietveld analyses shown in Figs. 1 a and b, the targets were $NiSb_2O_4$ (S_1) and $NiSb_2O_6$ (S_2), respectively, when the reaction temperature was 600 °C. However, it showed that the targets were composed of four crystalline phases. The impurity phases are Sb_2O_5 (main phase) [14], Sb_2O_3 [15] and NiO [16] for S_1; and Sb_2O_5, Sb_2O_3 and NiO for S_2. Table 1 shows that the main phase for S_2 is $NiSb_2O_6$. Figs. 1 c-f show that the main phase for all samples is $NiSb_2O_6$. Fig. 1c shows that the compound is still a composite with four crystal phases when nickle acetate was used as the raw material at 700 °C. However, the crystal phase purity was improved when nickle nitrate was used at this reaction temperature (Fig. 1d). The material is composed of three crystal phases.

However, it indicates that the impurity phase proportion in the total crystal phase amount (table 1), is small. Figs. 1 e and f show that the main crystal phase growth was excellent at 800 °C and the impurity crystal phase (Sb_2O_5) proportion was only about 3% for S_6.

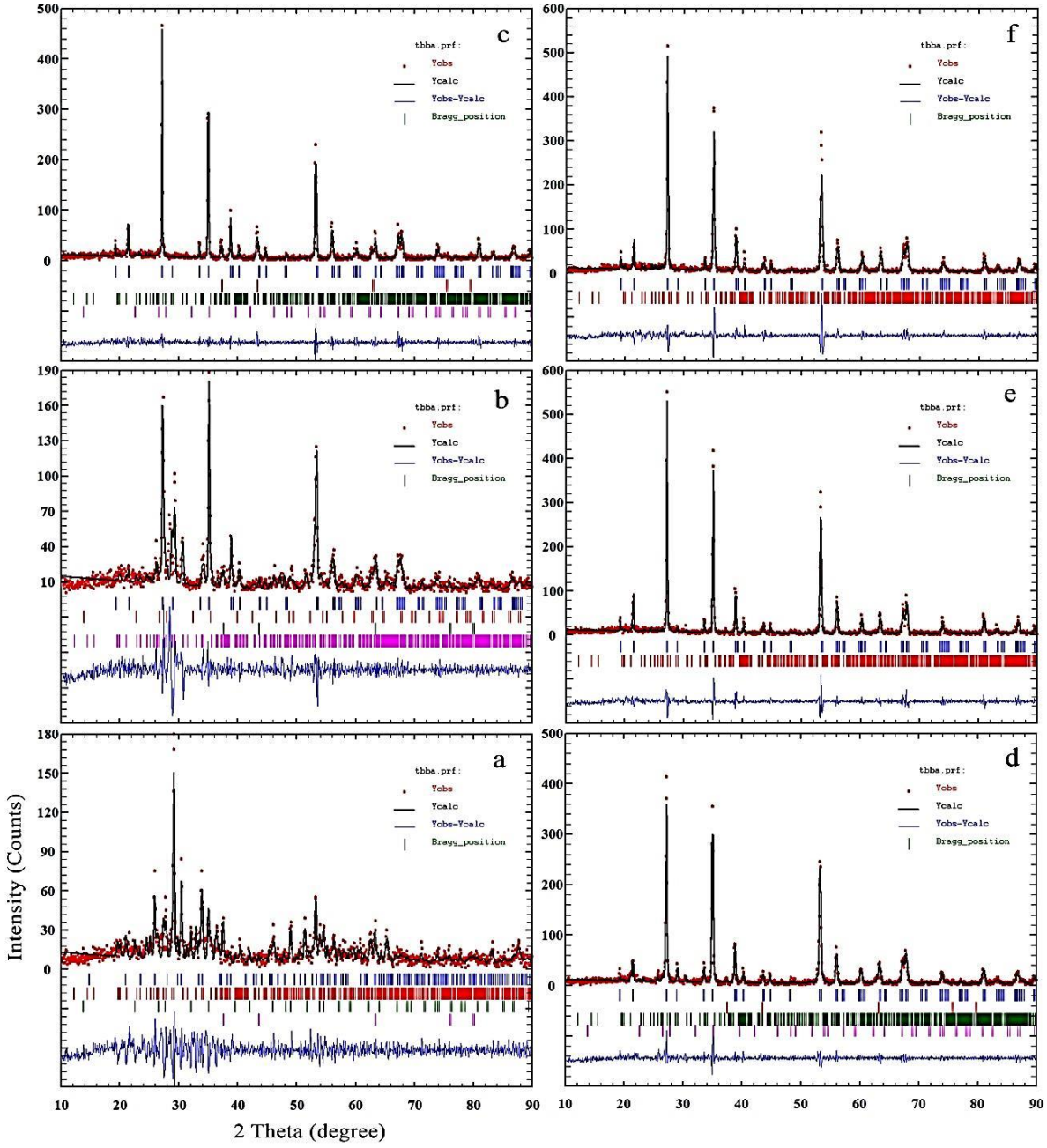

Fig. 1. XRPD patterns and the Rietveld analyses of a) S_1, b) S_2, c) S_3, d) S_4, e) S_5 and f) S_6.

The quantitative phase analysis was investigated with direct comparison method. In this method, we compared the experimental line intensity of the impurity phases from the mixture to a line from the main phase ($NiSb_2O_4$ or $NiSb_2O_6$) in the mixture. The phase comparison values are summarized in Table 1. It shows that the reaction temperature is the main factor in the crystal phase purity. So, the purity of the material increases with raising the reaction

temperature. Besides, the counts values are included in the table 1. The data shows that the crystal growth values of the targets for the main phase ($NiSb_2O_4$ or $NiSb_2O_6$) are considerably related to the reaction temperature. It shows that the obtained materials are crystallized better when the reaction temperature is increased from 600 °C to 800 °C. However, the data show that raw material type plays the role of another key factor in the crystal phase purity. It indicates that nickel nitrate is a better nickel source for the synthesis of pure $NiSb_2O_6$.

Table 2 shows the interplanar spacing (d) calculated from Bragg's equation and lattice parameters data obtained from Rietveld analyses, for S_2 to S_6. It was found that the d and lattice parameters values increased slightly by increasing the reaction temperature. Table 3 shows the crystal sizes of the as-synthesized nanomaterials ($NiSb_2O_6$) calculated by the Scherrer equation:

$$t = \frac{k\lambda}{B_{\frac{1}{2}} \cos\theta}$$

In this equation, t is the entire thickness of the crystalline sample, λ is the X-ray diffraction wavelength (0.154 nm), K is the Scherrer constant (0.9), $B_{1/2}$ of FWHM is the full width at half maximum intensity and θ is the half diffraction angle at which the peak is located. The data in Table 3 is in good agreement with the measured size distribution from FESEM images.

Table 1. Quantitative phase analysis for the obtained nanomaterials.

Sample	Rietveld parameters			Phase purity (%)	Counts
	R_{Bragg}	R_f	χ^2		
S_1	2.93	1.54	1.72	26	86
S_2	2.44	1.59	2.34	52	188
S_3	1.91	1.66	1.55	95	466
S_4	1.50	1.23	1.40	93	414
S_5	3.86	1.91	1.81	96	550
S_6	2.99	1.96	1.86	97	515

Table 2. Interplanar spacing (d) and cell parameters data for $NiSb_2O_6$ nanomaterials.

Sample	d (Å)	a (Å)	c (Å)	Volume(Å^3)
S_2	3.274	4.63108	9.19350	197
S_3	3.281	4.64133	9.22371	199
S_4	3.282	4.64275	9.23022	199
S_5	3.282	4.64237	9.22516	199
S_6	3.284	4.64421	9.22720	199

Table 3. Scherrer data information for $NiSb_2O_6$ nanomaterials.

Sample	2θ	$B_{1/2}$ (°)	$B_{1/2}$(rad)	cosθ$_B$	t(nm)
S_2	27.2073	0.24253	0.004231	0.971946	34
S_3	27.1479	0.15365	0.002680	0.972068	53
S_4	27.1409	0.16641	0.002903	0.972082	49
S_5	27.1395	0.23323	0.004069	0.972085	35
S_6	27.1301	0.22093	0.003854	0.972104	37

3-2- Morphology analysis

Figs. 2 and 3 show the FESEM images and particle size distribution profile of S_3 and S_4, respectively. Fig. 2 (a and b) shows the FESEM images of S_3. The images show that the morphology of the obtained material is composed of a spherical micron-sized structure. The sphere is composed of nano-particles. Besides, the image shows that the particle size and morphology of the particles are homogeneous. Fig. 3a shows the particle size distribution profile of S_3. It shows that the

maximum particle diameter size distribution is in the range of 20 – 25 nm. Figs. 2 c and d show the FESEM image of S_4. The images show that the material morphology has a nano-particle sized structure. It shows that the size and morphology of the particles are homogeneous. Fig. 3b shows the particle size distribution profile of S_4. The figure shows that the maximum particle diameter size distribution is in the range of 15 – 20 nm. According to the above mentioned data, we found that the raw material type at a certain temperature plays the role of a main factor in the morphology and particle size of the target.

Figs. 4 and 5 show the FESEM images and particle size profile distribution of S_5 and S_6, respectively. Fig. 4 (a and b) shows the FESEM images of S_5. Figs. 4 a and b show that the morphology of the obtained material is a porous structure. The images show that the porosity is composed of individual particles. Fig. 5a shows the particle size distribution profile of S_5. It shows that the maximum particle diameter size is in the range of 20 – 30 nm. Figs. 4 c and d show the FESEM image of S_6. It shows that the materials have a nano-particle sized structure. Fig. 5b shows the particle size distribution profile of S_6. The figure shows that the maximum particle diameter size is in the range of 40 – 50 nm. As it was mentioned before, we found that the raw material type is a main factor in the morphology and particle size of the target at a certain temperature. The particle size distribution profiles demonstrate that the maximum particle diameter sizes increased with raising the reaction temperature.

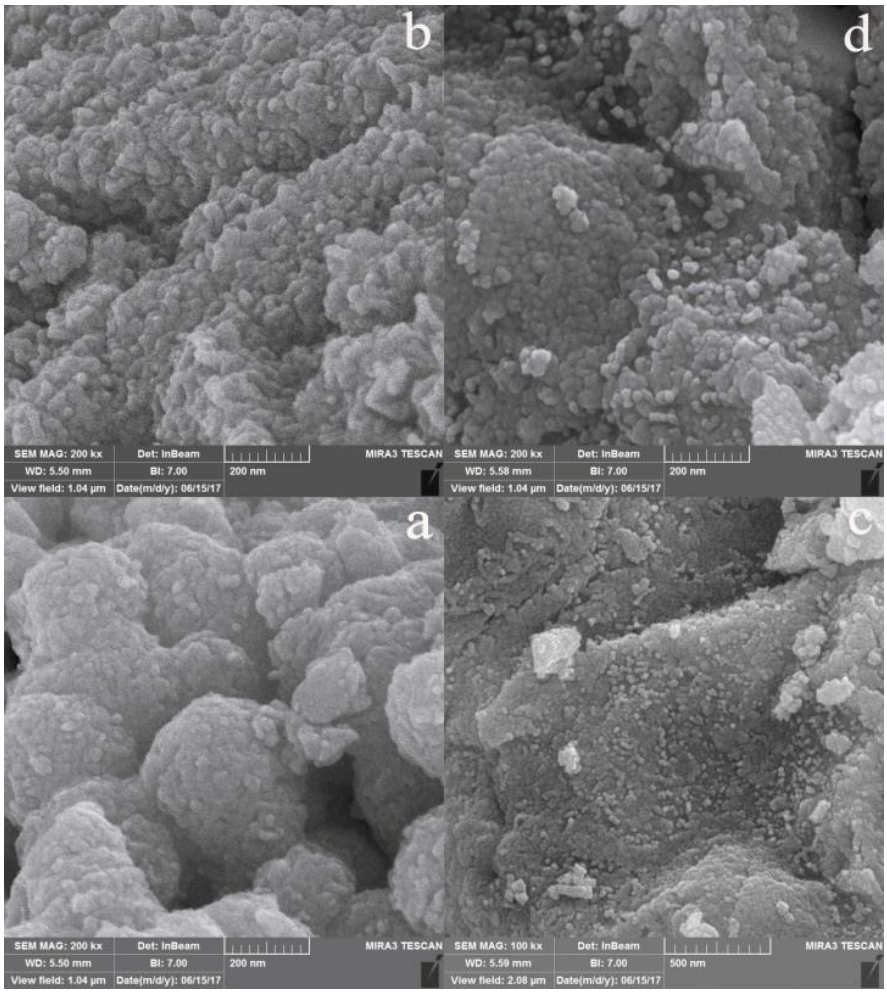

Fig. 2. FESEM images of S_3 and S_4.

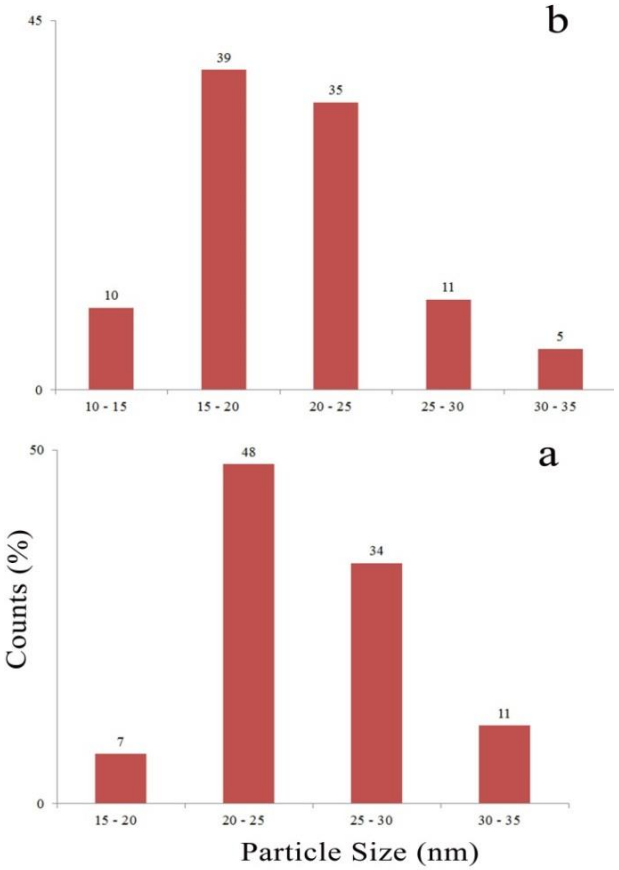

Fig. 3. Particle size distribution profiles of a) S_3 and b) S_4.

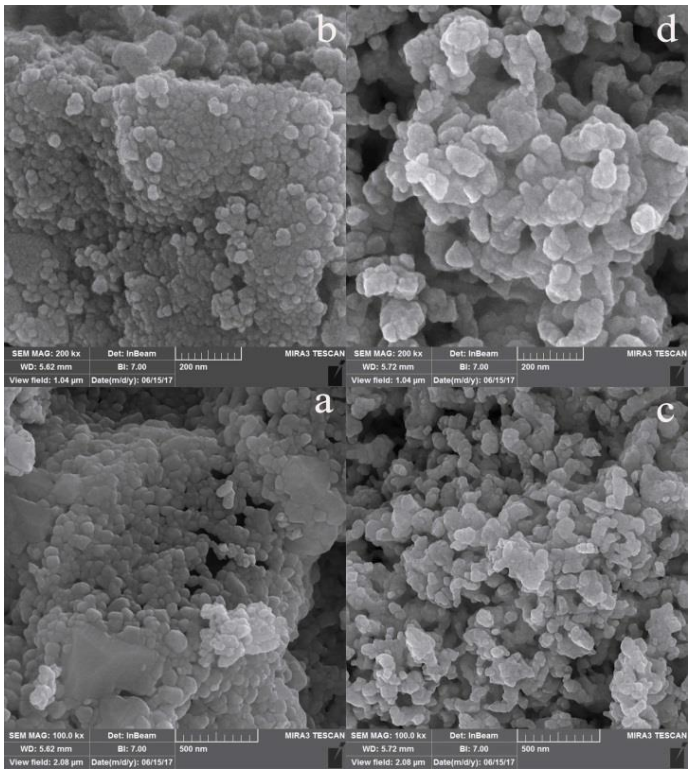

Fig. 4. FESEM images of S_5 and S_6.

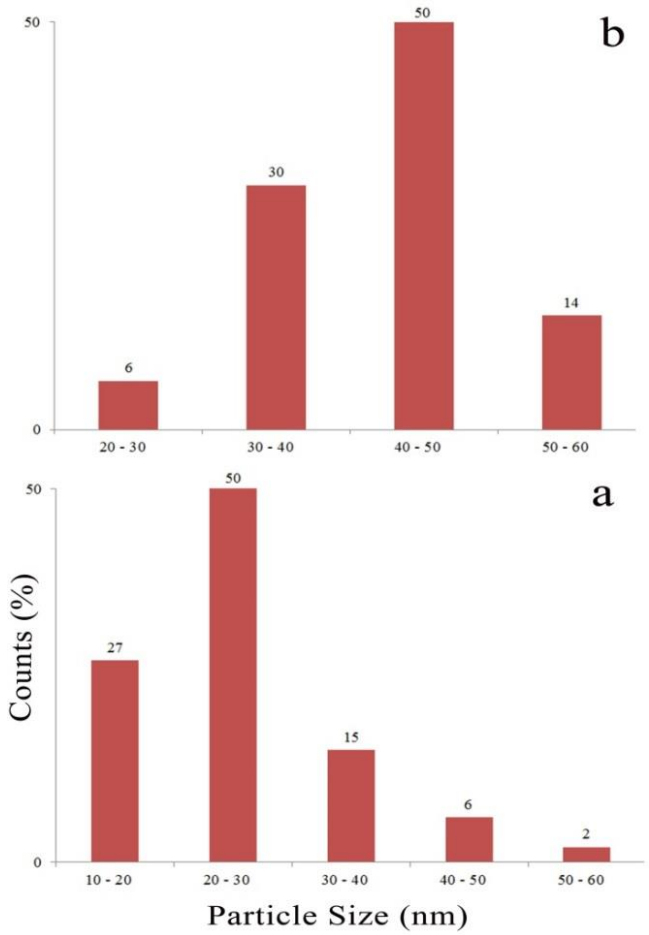

Fig. 5. Particle size distribution profiles of a) S_5 and b) S_6.

3-3- BET and BJH texture analysis

The synthesized powders were characterized for their surface area, average pore size, and average pore volume. Prior to N_2-physical adsorption measurement, the samples were degassed at 150 °C for 120 min in the nitrogen atmosphere. So, the specific surface area (S_{BET}) of the obtained materials was determined by adsorption-desorption isotherms of N_2 at 77 K. The surface area, pore volume, and average pore diameter of the synthesized materials are summarized in Table 4. From Table 5, it can be seen that the average surface area and pore volumes are about 5.312, 5.425, 6.125 and 4.872 m^2g^{-1}, and 0.033, 0.034, 0.035 and 0.031 cm^3g^{-1} for S_3, S_4, S_5 and S_6, respectively. Also, Table 5 shows the textural properties of the as-prepared materials. The data summarized in Table 5 shows that the specific surface area, pore diameter, and pore volume of S_4 is larger compared with S_3. Besides, the specific surface area, pore diameter for S_6 is smaller compared with S_5. The data show that reaction temperature and raw material type are the main factors in the physical properties of the targets.

Table 4. BET data for $NiSb_2O_6$ showing the textural properties of the obtained materials.

Sample	BET surface area (m^2g^{-1})	Pore diameter (nm)	Pore volume (cm^3g^{-1})
S_3	5.312	25.069	0.033
S_4	5.425	26.118	0.034
S_5	6.125	23.736	0.035
S_6	4.872	25.565	0.031

Table 5. BJH data for $NiSb_2O_6$ showing the textural properties of the obtained materials

Property	**S_3**	**S_4**	**S_5**	**S_6**
BJH surface area of pores	7.093	8.325	7.213	6.319
BJH volume of pores	0.034	0.036	0.037	0.032
BJH average pore width (4V/A)(nm)	19	17	18	20

3-4- Optical properties

Direct optical band gap energies of the synthesized $NiSb_2O_6$ nanomaterials calculated from UV-Vis absorption spectra are shown in Figs. 6a-d. According to the results of Pascual et al. [17], the relation between the absorption coefficient and incident photon energy can be written as $(\alpha h\nu)^2 = A(h\nu - Eg)$, where A and Eg are a constant and the direct band gap energy, respectively. The band gap energies were evaluated by extrapolating the linear part of the curve to the energy axis. It was found that the smallest direct optical band gaps were 2.70, 2.80 eV for S_3 and S_4; 2.90 and 2.80 eV for S_5 and S_6, respectively. According to the data, increasing the reaction temperature reduced the direct optical band gap energies of the targets. Because the purity of the targets increased at the reaction temperature of 800 °C, so we can conclude that the band gap energies for S_5 and S_6 are almost attributed to the pure $NiSb_2O_6$.

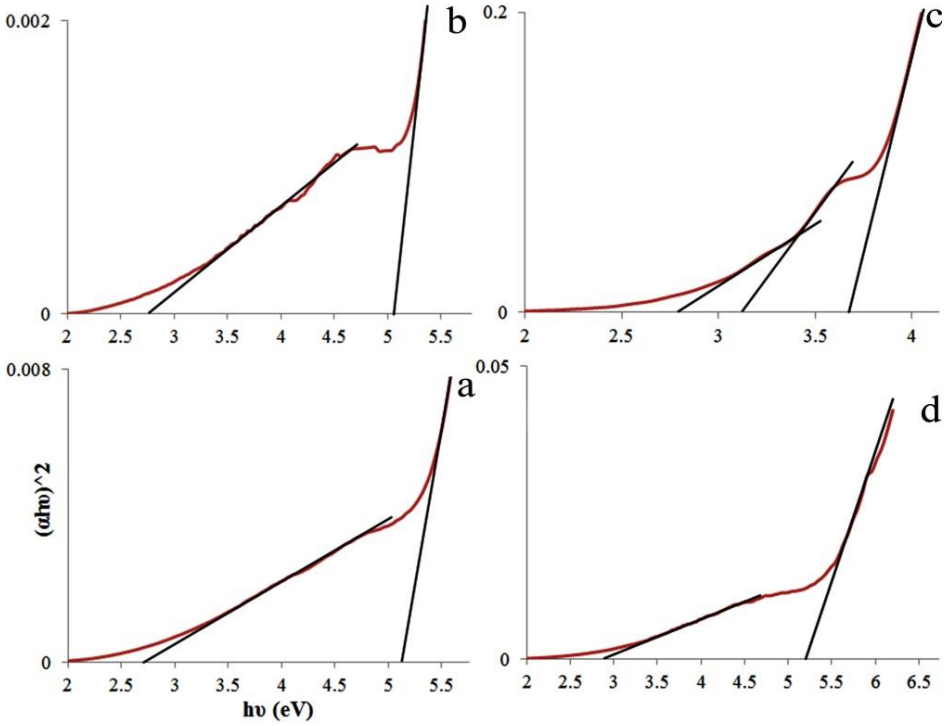

Fig. 6. Plots of $(\alpha h\nu)^2$ versus hν (eV) of a) S_3 and b) S_4, c) S_5 and d) S_6.

Figs. 7 a-d show the FTIR spectra of S_3 to S_6. There are some peaks at around 480, 530, 580, 680, 1390 and 3100 cm^{-1}. Peaks at 442, 530, 580 and 680 cm^{-1} are consistent with the bending vibration mode of Sb-O [18]. The peaks at around 1380 for S_3 and S_5 and 1394 for S_4 and S_6 are assigned to C=O and N-O stretching vibrations [19]. The peak at 3470 cm^{-1} is characteristic of O-H stretching, consistent with traces of water being present [20, 21].

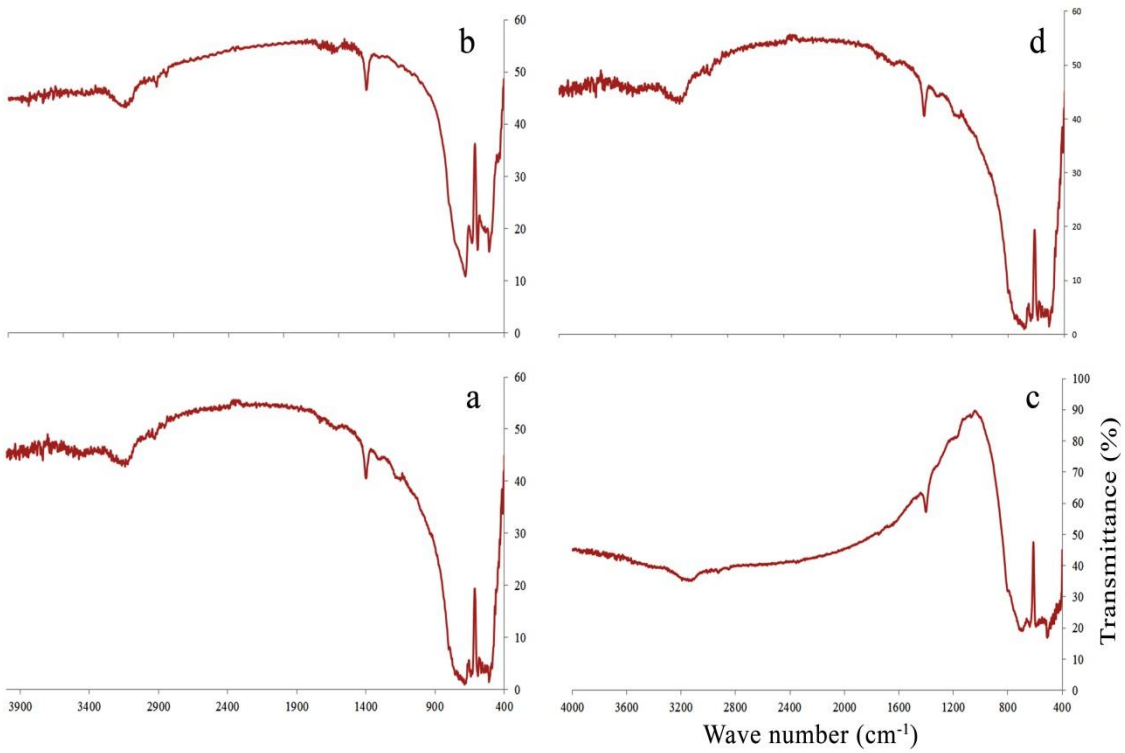

Fig. 7. FTIR spectra of a) S_3, b) S_4, c) S_5 and d) S_6.

4- Conclusion

In this work, $NiSb_2O_6$ nanomaterials were synthesized via solid state method. The XRPD patterns and structural analyses performed by the FullProf program employing profile matching showed that the synthesis was sucsessfull. The purity of the targets was also studied by the direct comparison method using the XRPD patterns. The Rietveld data revealed that the crystal phase purity of the as-synthesized nanomaterials increased with raising the reaction temperature from 600 to 800 °C. Besides, according to the data, the synthesis reactions using $Ni(NO_3)_2.6H_2O$ introduced a better crystalline growth and purity compared to $Ni(CH_3COO)_2.2H_2O$ raw material in a certain reaction temperature. FESEM images showed that the morphology of the targets was particle and porous. Also, the calculated direct optical band gap energies indicated that the band gaps decreased by increasing the reaction temperature from 600 to 800 °C. Because the purity of the targets increased at the reactionn temperature of 800 °C, we can conclude that the band gap energies for S_5 and S_6 are almost attributed to the pure $NiSb_2O_6$.

References

[1] A.Y. Nikulin, E.A. Zvereva, V.B. Nalbandyan, I.L. Shukaev, A.I. Kurbakov, M.D. Kuchugura, G.V. Raganyan, Y.V. Popov, V.D. Ivanchenko, A.N. Vasiliev," Preparation and characterization of metastable trigonal layered MSb_2O_6 phases (M = Co, Ni, Cu, Zn, and Mg) and considerations on $FeSb_2O_6$", Dalton Trans., 2017. DOI: 10.1039/c6dt04859e.

[2] K. Swaminathan, O.M. Sreedharan," Potentiometric determination of stabilities of $NiSb_2O_4$ and $NiSb_2O_6$", J. Alloys Compd., Vol. 292, 1999, pp. 100-106.

[3] S. Jiao, G. Pang, H. Liang, Y. Chen, S. Feng," Hydrothermal synthesis and magnetic properties of $CuSb_2O_6$ nanoparticles and nanorods", J. Nanopart. Res., Vol. 9, 2007, pp. 605.

[4] A. Singh, A. Singh, S. Singh, P. Tandon," Nickel antimony oxide ($NiSb_2O_6$): A fascinating nanostructured material for gas sensing application", Chem. Phys. Lett., Vol. 646, 2016, pp.41-46.

[5] G. Westin, M. Nygren," Sol-Gel Preparation of M-Sb oxides from Sb (OBu"), -M-Acetate precursors with M = Mn, Co, Ni", J. Mater. Chem., Vol. 3, 1993, pp. 367-371.

[6] J. Singh, N. Bhardwaj, S. Uma,'" Single step hydrothermal based synthesis of M(II)Sb_2O_6 (M = Cd and Zn) type antimonates and their photocatalytic properties", Bull. Mater. Sci., Vol. 36, 2013, pp. 287-291.
[7] D. Larcher, A.S. Prakash, L. Laffont, M. Womes, J.C. Jumas, J. Olivier-Fourcade, M.S. Hedge, J.M. Tarascon," Reactivity of Antimony Oxides and MSb_2O_6, M = Cu, Ni, Co…, Trirutile-type Phases with Metallic Lithium", J. Electrochem. Soc., Vol. 153, 2006, pp. 1778-1787.
[8] H. Ehrenberg, G. Wltschek, J. Rodriguerz-Carvajal, T. Vogt," Magnetic structure of the tri-rutiles $NaTa_2O_6$ and $NiSb_2O_6$", J. Magn. Magn. Mater., Vol. 184, 1998, pp. 111-115.
[9] H.G. Bonilla, V.M.R. Betancourtt, J.T.G. Bonilla, M.F. Mortinz, A.G. Bonilla, M.A. Gonzalez, S.S.S. Salazar, L.G. Ortiz," Synthesis and characterization of Nanostructured $NiSb_2O_6$ powders. IX International conference in surfaces", materials and vacuum. September 26 th – 30 th, Mexico. 2016. Page 259.
[10] Y. Hanifehpour, B. Mirtamizdoust, M.A. Cheney, S.W. Joo," Facile synthesis, characterization and BET study of neodymium doped spinel Mn_3O_4 nanomaterial with enhanced photocatalytic activity", J Mater Sci: Mater Electron., Vol. 28, 2017, pp. 11654–11664.
[11] Y. Hanifehpour, N. Hamnabard, B. Mirtamizdoust, S.W. Joo," Sonochemical Synthesis, Characterization and Sonocatalytic Performance of Terbium-Doped CdS Nanoparticles," J. Inorg. Organomet. Polym., Vol. 26, 2016, pp. 623–631.
[12] J.W. Lee, J.K. Lee, S.K. Cho, J.S. Jung, S.H Lee," Partial Oxidation of Methane over M-Sb-Te-O (M = Transition Metal) Catalysts ", Bull. Korean Chem. Soc., Vol. 25, 2004, pp. 573-576.
[13] S.Z. Alabdeen, I. Ismail," Studying the Structural Changes of $NiSb_2O_4$ by Temperature Using Sol-Gel Method", Chem. Mater. Res., Vol. 8, 2016, pp. 13-17.
[14] M. Jansen," Die kristallstruktur von antimony (V)-oxid", Acta Crystallogr., Sect. B., Vol. 35, 1979, pp. 539-542.
[15] M.J. Buerger, S.B. Hendricks," The crystal structure of valentinite", Zeitschrift fur Kristallographie., Vol. 98, 1938, pp. 1-30.
[16] A. Leineweber, H. Jacobs, S. Hull," Ordering of nitrogen in nickel nitride Ni_3N determined by neutron diffraction", Inorg. Chem., Vol. 40, 2001, pp. 5818-5822.
[17] J. Pascual, J. Camassel, M. Mathieu," Fine structure in the intrinsic absorption edge of TiO_2", Phys. Rev. B: Solid State, 18, 1978, pp. 5606-5614.
[18] S.G.X. Yang, Q. Shao, Q. Liu, T. Wang, L. Wang, X. Wang," Self-assembled flower – like antimony trioxide micro structures with high infrared reflectance performance. J. Solid State Chem., Vol. 200 2013, pp. 136-142.
[19] L. Song, S. Zhang, Q. Wei," Antimony trioxide microstructures: 3D grass-like architectures and optical properties", Chem. Eng. J., Vol. 179, 2012, pp. 40- 411.
[20] L. Zhang, Y. Lin, R. Li, F. Zhang," Layered double hydroxides used as flame retardant for engineering plastic acrylonitrile–butadiene–styrene (ABS) Sailong", J. Phys. Chem. Solids., Vol. 73, 2012, pp. 1514-1517.
[21] Z. Deng, D. Chen, F. Tang, J. Ren, A.J. Muscat," Synthesis and Purple-Blue Emission of Antimony Trioxide Single-Crystalline Nanobelts with Elliptical Cross Section", Nano Res., Vol. 2, 2009, pp. 151-160.